

# An Algorithm for Estimation of Wave Height From Shadowing in X-Band Radar Sea Surface Images

Rune Gangeskar

**Abstract**—Directional wave spectra and integrated wave parameters can be derived from X-band radar sea surface images. The calibration of such spectra has until now depended on various empirical and semiempirical methods, which also require an external reference increasing the total expenses of operation. A novel algorithm, which is fully based on theory, producing reasonable estimates of the significant wave height based on shadowing in the images, has been now developed. The method does not require any reference measurements, and with that, enables automatic calibration of spectra from radar sea surface images, as well as the potential for reduced operational cost and increased accuracy of such wave-monitoring systems. Promising results are obtained with data acquired at a test site in the North Sea. Further work is, however, required to refine the algorithm and to test it under varying circumstances at various sites.

**Index Terms**—Image analysis, radar, sea surface, shadowing, wave height.

## I. INTRODUCTION

**D**IRECTIONAL wave spectra can be estimated by comprehensively processing X-band radar sea surface images [1]–[3]. Until now, however, calibration of such wave spectra has depended on various empirical and semiempirical methods, such as, for instance, by using the signal-to-noise ratio in spectra based on the dispersion filtering process [4] and [5]. For this procedure, an external reference, for instance, a wave buoy, is required to establish certain calibration parameters for the particular system of interest. Other calibration approaches are based on image statistics related to various physical processes, such as, for instance, the approaches described in [6]–[12]. These also require input from an external reference to initially establish the relation between wave heights and statistical parameters for the particular system geometry. In addition to such empirical and semiempirical methods, it is also possible to continuously calibrate using an external reference.

Several attempts have been made to utilize information about shadowed areas in radar images to calibrate wave spectra. A concept based on geometric optics and a constant threshold probability of illumination  $P_0$  [8] was further developed in [9]. In [10]–[12], however, it was shown that assuming a constant value of  $P_0$  did not produce reasonable wave height estimates

for various geometries and sea states, and an improved algorithm with a varying  $P_0$  was introduced in [11]. A limited part of the variance of  $P_0$  was theoretically explained by simulations in [12]. According to [12], it is now possible to estimate the significant wave height  $H_{m0}$  with reasonable accuracy using this approach, although the method is still empirical and requires input from an external reference for initial calibration.

It should also be mentioned that there is a discussion going on whether total shadowing of local surface areas, as explained by the theory of geometric optics, really exists when considering microwave backscatter from the ocean. A study and discussion on this topic is provided in [13], in which their results fit more within the frames of a partial shadowing model than a geometric shadowing model. Their explanation is that surface areas hidden behind other parts of the surface also contribute to the backscatter to some extent, due to diffraction of some of the electromagnetic signal. For many practical purposes, however, it may be difficult to determine whether radar images are influenced by total (geometric) shadowing or partial shadowing, because the differences between those two cases may be very small, depending on the signal level compared to the noise level, as well as geometric factors and radar properties.

This paper describes a novel algorithm that produces reasonable estimates of  $H_{m0}$  based on shadowing in X-band radar images. The method is fully based on theory and does not require any reference measurements, which is not the case for any other known calibration method. The method is derived from principles of geometric shadowing, and the results indicate that these principles make an adequate description of the actual and underlying physics of the imaging process for the data used in this work.

## II. METHOD

The algorithm consists of the following main steps:

- Estimation of the gray-level threshold that separates shadowed image areas from remaining areas.
- Image thresholding and calculation of the ratio of shadowing in local image areas.
- Estimation of the root-mean-square (RMS) surface slope by fitting Smith's function [14].
- Estimating  $H_{m0}$  from the RMS surface slope and the mean zero up-crossing period  $T_{m02}$  [15] and [16].

### A. Estimation of the Gray-Level Shadow Threshold

Estimating the gray-level shadow threshold is one of the two key parts of the algorithm. This threshold is used to separate shadowed image areas from remaining areas, as illustrated for data set A in Figs. 1 and 2, making it possible to calculate local

Manuscript received February 11, 2013; revised June 4, 2013; accepted July 1, 2013. Date of publication July 24, 2013; date of current version February 27, 2014. This work was supported by Miro AS.

This paper has supplementary downloadable material available at <http://ieeexplore.ieee.org>, provided by the author. This includes four GIF animations for improved visualization of the relation between radar image, edge image, and shadow image. This material is 461 kB in size.

The author is with Miro AS, 1383 Asker, Norway, and also with Tronrud Engineering AS, 3514 Ringerike, Norway (e-mail: [rune.gangeskar@broadpark.no](mailto:rune.gangeskar@broadpark.no)).

Digital Object Identifier 10.1109/TGRS.2013.2272701

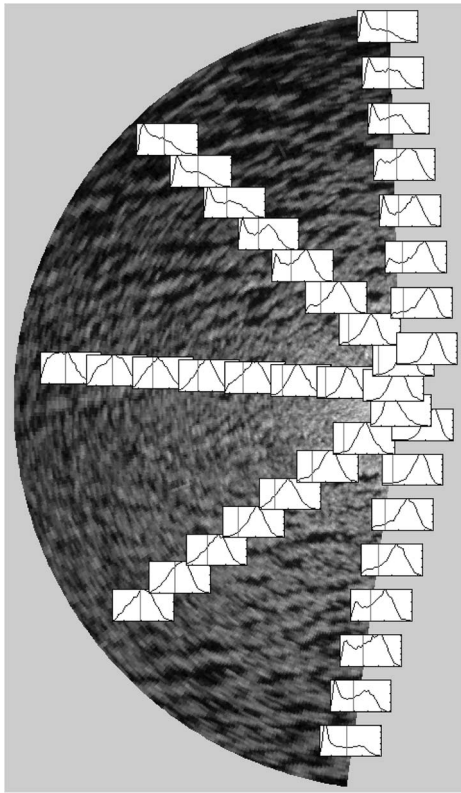


Fig. 1. Radar image from data set A with local gray-level histograms and the shadow threshold indicated with gray lines. Significant wave height  $H_{m0}$  is approximately 4 m, and wind speed is approximately 15 m/s.

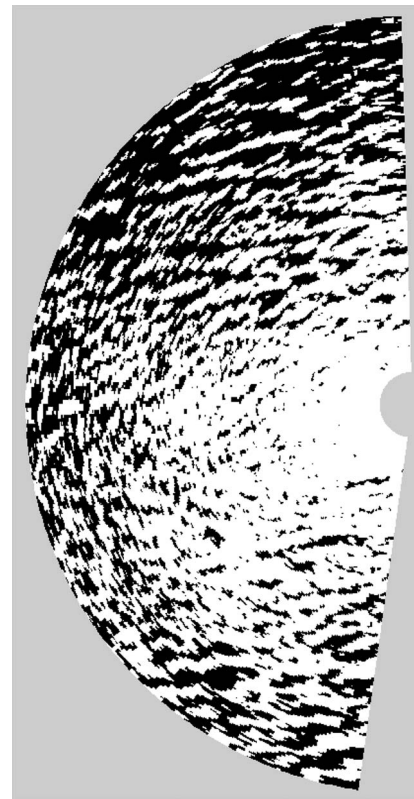


Fig. 2. Shadow image corresponding to the radar image in Fig. 1 (data set A). Shadows are black.

shadowing ratios in the image. The other key part is the fitting of Smith's function described in a later section.

One motivation for starting this work was that the contribution to the first-order local image statistics from shadowed areas was observable in local histograms [17]. It became, however, evident that only histograms do not provide enough information to automatically estimate the shadow threshold with sufficient accuracy. Both local (such as the histograms in Fig. 1) and global histograms were thoroughly inspected, but neither visual inspection nor methods of adaptive threshold estimation gave stable and reasonable values for the shadow threshold. The possibility to utilize the accuracy of fitting Smith's function described later in this paper was also examined, but without obtaining the required accuracy. Then, an alternative strategy was investigated: direct detection of shadowed areas in the image. Various methods based on roughness and edges were considered [18], as well as relaxation [19]. The most successful method was based on edge detection and statistics of the edge image, and this will be described in the following. The steps of this method are:

- Calculating edge images using pixel difference operators.
- Filtering to disregard areas located too far away from possible shadow.
- Noise filtering based on number of directions.
- Calculating the mode of the edge statistics histogram.

The method shares some properties with the method in [20], but it is also different due to the filtering and because simple pixel difference operators are used instead of a Laplacian operator.

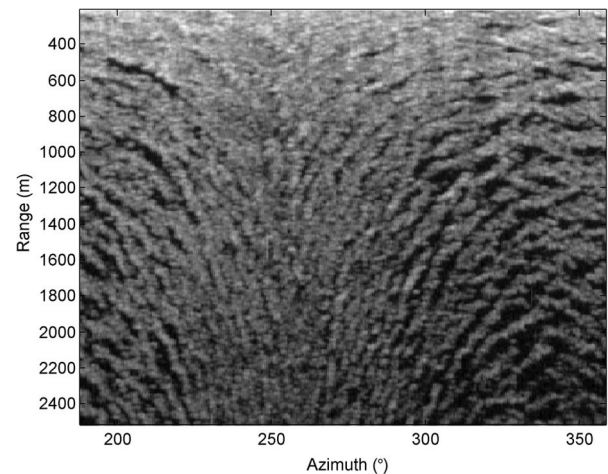


Fig. 3. Raw radar image (data set A) in Cartesian coordinates.

1) *Calculating Edge Images:* The radar image in Fig. 1 (data set A) is shown in Cartesian coordinates in Fig. 3. Shadowed areas are visible as relatively uniform and dark areas (see Fig. 4). The idea of applying edge detection to the radar image is that the transition between shadow and no shadow in the image typically will correspond to more distinct edges than edges produced by the continuously varying gray levels due to gravity wave modulation of the backscattered electromagnetic signal. Such transitions probably can be also found if the image is influenced by a partial shadowing process instead of a geometric shadowing process, as discussed in [13], because the backscatter from hidden areas due to diffraction will be limited

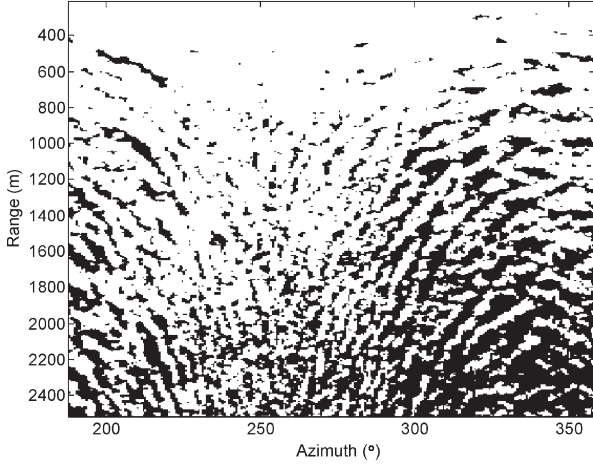


Fig. 4. Shadow image obtained by thresholding the radar image. Shadows are black.

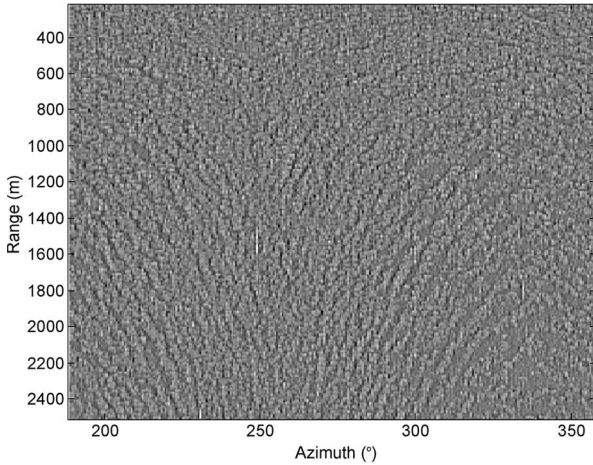


Fig. 5. Sum of eight edge images corresponding to the eight simple pixel difference operators (data set A).

compared to the direct backscatter from visible areas. Shadow edges are precisely marked out by convolving the radar image with simple pixel difference operators [18] for eight neighbors. As an example, the convolution with the simple pixel difference operator for the right-hand neighbor is given by

$$I_{E1}(r, \theta) = I(r, \theta) \otimes H_1(r, \theta) \quad (1)$$

$I(r, \theta)$  is the raw radar image, which is a function of range  $r$  and azimuth angle  $\theta$ , and  $I_{E1}(r, \theta)$  is the resulting edge image indicating edges in the leftward direction. The pixel difference operator is given by

$$H_1(r, \theta) = \begin{bmatrix} 0 & 0 & 0 \\ 0 & 1 & -1 \\ 0 & 0 & 0 \end{bmatrix}. \quad (2)$$

Fig. 5 shows the sum of all eight edge images, i.e.,  $I_{E1}(r, \theta)$  to  $I_{E8}(r, \theta)$ , to illustrate edges of the wave pattern. The edges are more easily visible after performing thresholding in the next step. Note that some distinct radial noise lines are visible in the edge image, indicating that a noise line removal, as described in [21], could be applied in advance of applying this algorithm to radar images.

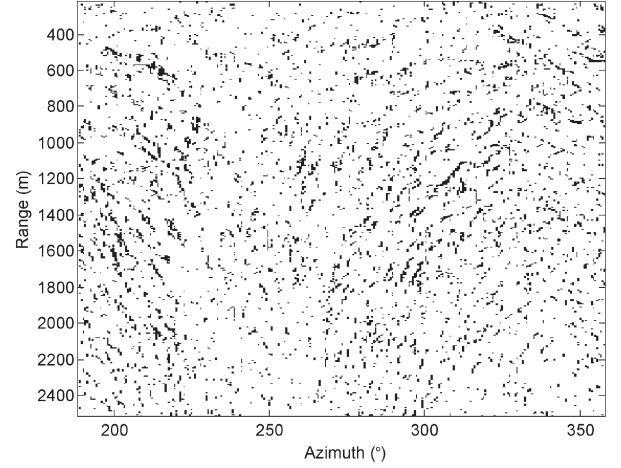


Fig. 6. Combination of eight edge images after thresholding. Edges are black.

More complex operators that also include averaging [18] have been considered. The simplest and most precise operators have, however, outperformed the larger and more complex ones so far because it is of high importance to precisely locate the edges. For the same reason, noise filtering, such as median filtering, applied to the image before applying pixel difference operators did not improve the accuracy of the final threshold estimate.

The edge images are thresholded using a threshold value equal to the upper  $N$ -percentile of the pixels. Thresholding of edge image number  $i$  is given by

$$I_{Ti}(r, \theta) = \begin{cases} 1, & I_{Ei}(r, \theta) > \text{upper } N\text{-percentile} \\ 0, & \text{otherwise.} \end{cases} \quad (3)$$

Then, the eight edge images are combined into one single edge image (see Fig. 6) by the following two step procedure:

$$I_T(r, \theta) = \sum_{i=1}^8 I_{Ti}(r, \theta) \quad (4)$$

$$I_F(r, \theta) = \begin{cases} 1, & I_T(r, \theta) \in [1, \tau_F] \\ 0, & \text{otherwise.} \end{cases} \quad (5)$$

Thresholding using values of  $\tau_F$  less than 8 makes removal of single pixel noise possible, as described below. In Fig. 6, however,  $\tau_F = 8$  to illustrate the effect of filtering in the next processing step.  $N = 10$  and pixels exceeding the threshold are black.

One question that should be further investigated is how the azimuth and range resolution of the image relative to the actual resolution of the radar influence the edge detection process. Consider a digitized radar image with a range resolution significantly higher than the radar range resolution, but with the image azimuth resolution equal to or less than the radar azimuth resolution. In this image, transitions between shadow and no shadow will appear less distinct in the range dimension than in the azimuth dimension and, hence, produce lower values in the edge image. In such situations, some sort of normalization may be necessary to get comparable statistics in all directions.

2) *Filtering*: The edge images are filtered to eliminate edges located too far away from possible shadow. Areas of possible shadow are defined by means of their location in the radar



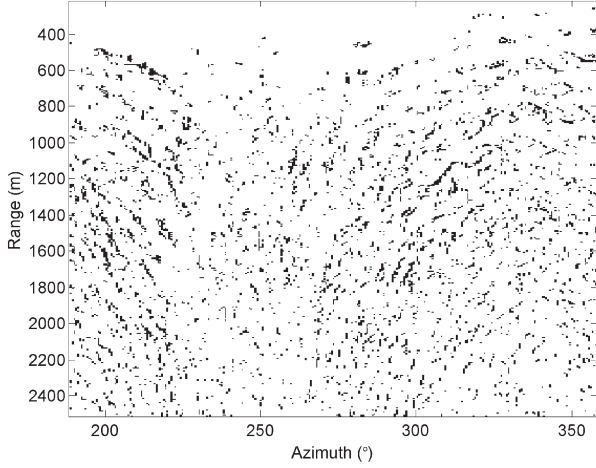


Fig. 7. Combination of eight edge images after thresholding and filtering. Edges are black.

image histogram. Based on experience with real data, shadow gray levels typically should be located among the lower 30% of the image pixels.

Single pixel noise is removed by requiring the number of edge directions for one single pixel to be less than a certain threshold. If, for instance, one pixel has edges in all eight directions, it means that this pixel is not connected to other pixels with a low gray level. Such single pixels may of course be due to small shadows, but disregarding them does not lead to significant loss of information, and it may remove significant amounts of noise.

Fig. 7 shows the result of filtering the edge image as described, using  $\tau_F = 5$ . The difference is significant, particularly at short ranges where the strong electromagnetic backscatter produces relatively sharp edges not being related to shadowing.

3) *Calculating the Histogram Mode:* The edge image now can be used to identify which pixels are located on the transition between shadow and no shadow in the radar image. For every single 1 in the edge image, the corresponding pixel value  $\eta$  from the radar image is used to create a histogram  $F_H(\eta)$  of the statistics of image pixels located between shadow and no shadow.  $F_H(\eta)$  for data set A is illustrated in Fig. 8 (black line) together with the distribution for the entire image (gray line). Then, finally, the histogram mode defines the gray-level shadow threshold  $\tau_S$  (dash line in Fig. 8) as follows:

$$\tau_S = \text{mode}(F_H(\eta)). \quad (6)$$

### B. Calculating Shadowing Ratio

The radar image is thresholded, using the threshold  $\tau_S$  defined in the previous section, so that pixels corresponding to shadow (with values less than the threshold) get the value 1 and the remaining pixels get the value 0, as illustrated in Fig. 2 (polar coordinates) and in Fig. 4 (Cartesian coordinates), as follows:

$$I_S(r, \theta) = \begin{cases} 1, & I(r, \theta) < \tau_S \\ 0, & \text{otherwise.} \end{cases} \quad (7)$$

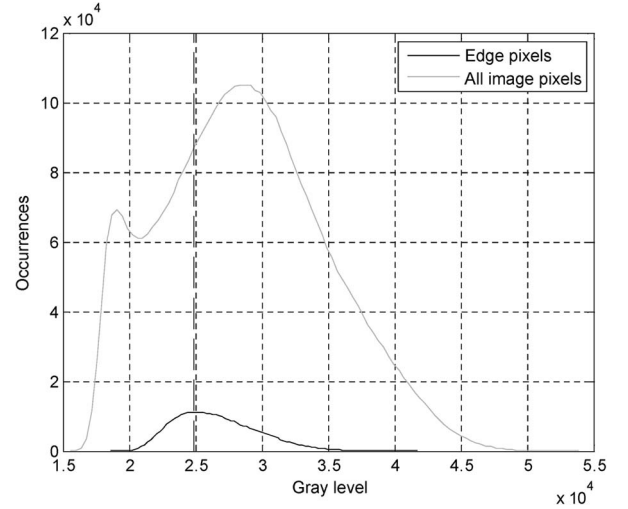


Fig. 8. Distribution of image pixels located between shadow and no shadow (black) compared with distribution of all image pixels (gray). Shadow threshold indicated by dash line.

The shadow image  $I_S(r, \theta)$  is divided into sectors, and the ratio of shadowing as a function of grazing angle  $S(\gamma)$  is calculated for each sector.

### C. Estimation of Surface Slopes

This part of the work depends on theory of geometric shadowing of random rough surfaces [5] and [22]. The 2-D theory in [22] makes utilization of certain types of nonisotropic surface statistics possible, which is expected to be an advantage when analyzing direction-dependent sea surface characteristics. Still, the advantages of the one-dimensional (1-D) theory are considered more important. As discussed later, this theory brings along possibilities for performing various sorts of quality control. Moreover, a large amount of the nonisotropic characteristics being intercepted by the 2-D theory can be accounted for in the 1-D theory. This is done by combining quality control and averaging of the mean-square slopes obtained by the 1-D theory over the azimuth dimension. In both cases, direct estimation of the surface RMS slope is possible, and the 1-D special case of the 2-D theory in [22] produces results identical to the theory in [14].

A mathematical expression for the relation between the illumination  $L(\gamma) = 1 - S(\gamma)$  and the RMS slope  $\sigma_{\text{RMS}}$  of a random rough surface described by a 1-D Gaussian surface height probability function has been previously derived [14] as follows:

$$L(\gamma) = \frac{1 - 1/2 \operatorname{erfc}(\mu/\sqrt{2}\sigma_{\text{RMS}})}{\Lambda(\mu) + 1}, \quad (8)$$

where

$$\Lambda(\mu) = \frac{\sqrt{2/\pi} \cdot \sigma_{\text{RMS}} / \mu \cdot e^{-\mu^2/2\sigma_{\text{RMS}}^2} - \operatorname{erfc}(\mu/\sqrt{2}\sigma_{\text{RMS}})}{2} \quad (9)$$

and

$$\mu = \tan(\gamma). \quad (10)$$

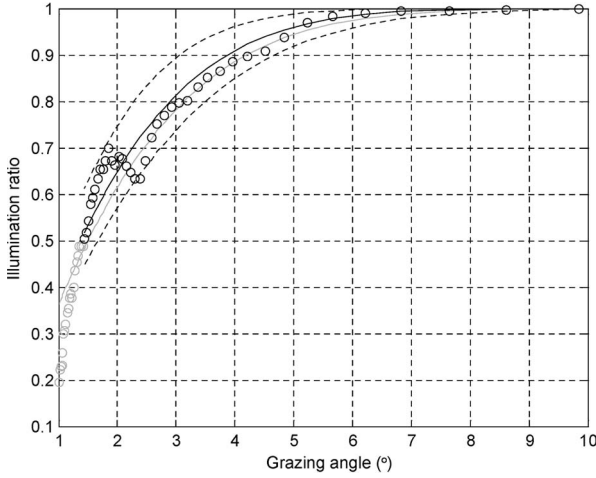


Fig. 9. Illumination as a function of grazing angle for one single azimuth direction in data set A. The measured data points of local illumination ratios are indicated with circles and the fitted Smith's function with a solid line. Dotted lines indicate an absolute RMS slope deviation of  $\pm 1\%$  from the best fit. Gray color indicates all data, and black color indicates data used after limiting the image in accordance with the system range.

Erfc is the Gauss error function (or probability integral). The Gaussian surface height probability function used to derive the previous mathematical expression is given by

$$P(\xi)\Delta\xi = \frac{1}{\sqrt{2\pi}\nu} e^{-\xi^2/2\nu^2} \Delta\xi, \quad (11)$$

which provides the density of surface height variations  $\xi$  from the mean plane, where  $\nu$  is the RMS height deviation. Gaussian surface height probability functions often provide reasonable descriptions of real sea surfaces [15], [22] and [16]. Equation (8) is referred to as Smith's function throughout this paper. Note that  $L(\gamma)$  is the probability for an area to be illuminated.

An example of the illumination as a function of grazing angle for one single azimuth direction is shown in Fig. 9 (circles), as well as Smith's function fitted to the data (solid line). By fitting Smith's function, an estimate of  $\sigma_{\text{RMS}}$  is obtained. Dotted lines indicate an RMS slope deviation of  $\pm 1\%$  (absolute) from the best fit to illustrate the sensitivity of the fit. The fit is performed using the Nelder–Mead simplex method in MATLAB [23]. The measured data fit well with Smith's function, taking into account that only one parameter (and degree of freedom) is fitted. This also indicates that the principles of geometric optics make an adequate explanatory model for our purpose. A corresponding plot for every tenth degree of azimuth angle is shown in Fig. 10. Here, the data in Fig. 9 are located to the left at the highest grazing angle, and the dotted lines are omitted to improve the readability.

Note that the illumination ratio in (8) can be integrated over all grazing angles (or ranges) within one azimuth sector, giving the relation between the shadowing ratio and the slope. This, however, provides no more information than we already have, and the possibility to use information from the fitting of Smith's function will be lost.

After estimating  $\sigma_{\text{RMS}}$  for various azimuth angles  $i$ , an average RMS slope  $\sigma_{\text{RMS}}^A$  can be defined by averaging the

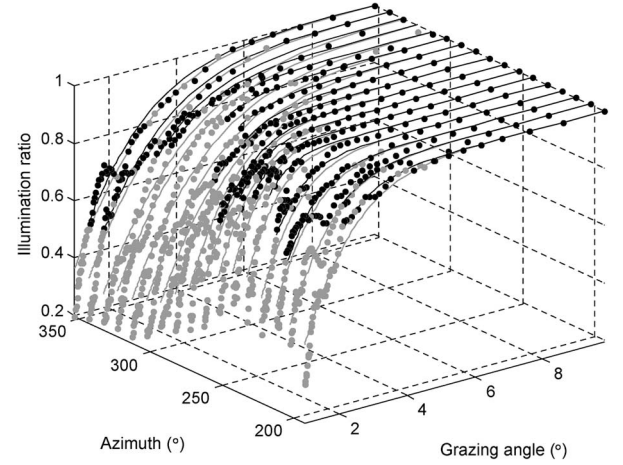


Fig. 10. Illumination as a function of grazing angle for 17 different azimuth directions. Gray color indicates all data, and black color indicates data used after limiting the image in accordance with the system range.

mean-square slopes for all single azimuth directions as follows:

$$\sigma_{\text{RMS}}^A = \sqrt{\frac{1}{M} \sum_{i=1}^M \sigma_{\text{RMS}i}^2} \quad (12)$$

where  $M$  is the number of directions.

1) *Situations With Weak Signal:* A large amount of the available data fits well to Smith's function, as demonstrated in the previous example. However, several problems have been observed, primarily associated with low wind speeds.

The most frequently occurring problem is due to the backscattered electromagnetic signal falling off at significantly shorter ranges than the outer image edge. This causes an overestimation of the shadowing ratio at longer ranges. This is not a problem for data set A considered previously, because the wind speed is sufficiently high (approximately 15 m/s). In Fig. 9, a dropoff is barely visible for the lowest grazing angles where the algorithm automatically disregards some data points when fitting Smith's function. In Fig. 10, however, it can be observed that the number of data points automatically disregarded is larger for some azimuth directions, depending on sea surface characteristics and wind fluctuations.

Fig. 11 shows an example of the illumination ratio and Smith's function for one single azimuth direction for a data set with less wind (data set B). The wind speed is approximately 4 m/s, and  $H_{m0}$  is approximately 2 m. Here, the reduction in the estimated illumination ratios caused by a drop in the sea backscatter is clearly visible. This again causes the RMS slope  $\sigma_{\text{RMS}}$  and  $H_{m0}$  to be overestimated if using all data (gray color). Smith's function cannot be properly fitted to these data without disregarding data at longer ranges, as shown with black color. Figs. 12 and 13 show corresponding radar and shadow images in Cartesian coordinates, respectively. The overestimated amount of shadowing at longer ranges due to the weak backscatter is clearly visible. Lowering the shadow threshold would not improve the situation, because real shadows at short ranges then would be lost. A range-dependent shadow threshold might improve the situation, although it would not make recovery of lost information due to weak signal possible.

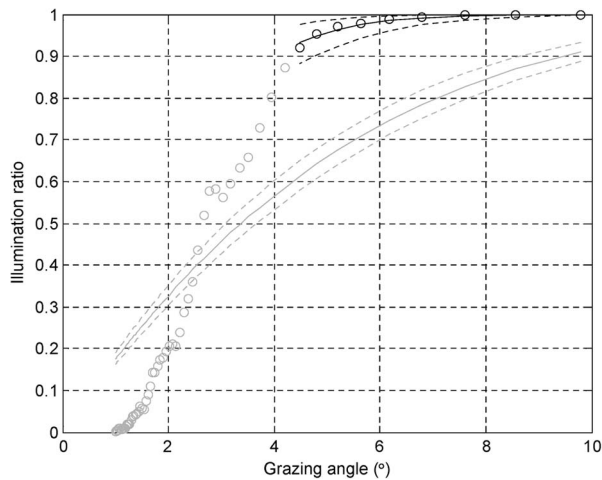


Fig. 11. Illumination as a function of grazing angle for one single azimuth direction in data set B. Measured data points of local illumination ratios are indicated with circles and the fitted Smith's function with solid lines. Dotted lines indicate a deviation of  $\pm 1\%$  (absolute) from the best fit of the RMS slope. Gray color indicates all data, black color indicates data used after limiting the image in accordance with the system range.  $H_{m0}$  is approximately 2 m, and wind speed is approximately 4 m/s.

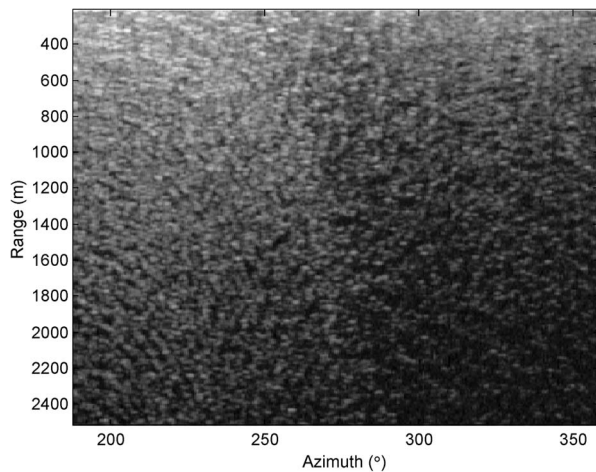


Fig. 12. Raw radar image with lower signal (data set B).

The radar image is automatically limited in range so that only image pixels at ranges with a sufficiently strong sea backscatter are used in the calculations. The transition range between a too weak signal and a sufficiently strong signal is referred to as the system range in this paper. Various values of the system range are examined for the azimuth direction of interest, and the one giving the lowest value of  $\sigma_{RMS}$  (and therefore also  $H_{m0}$ ) is selected. The rationale for this can be understood by a closer inspection of the data in Fig. 11. By gradually decreasing the system range from full range (moving in the direction of increasing grazing angles), the fit of Smith's function gradually will produce lower values of  $\sigma_{RMS}$  until the areas of weak signal is omitted from the calculation. The elimination of data should, however, be limited to ensure that there are enough data left to perform a reasonable fit of Smith's function. A minimum number of remaining data points is required, as well as a minimum variation of the illumination ratio below 1.

If a slope minimum is not found above the minimum system range required for a reliable fit, an extrapolation may, in some

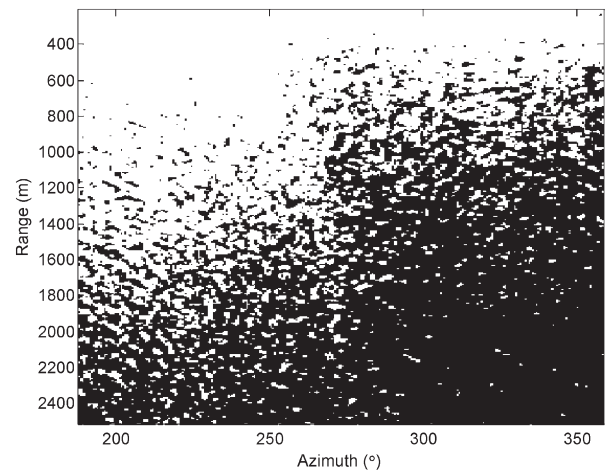


Fig. 13. Shadow image corresponding to the radar image above (data set B).

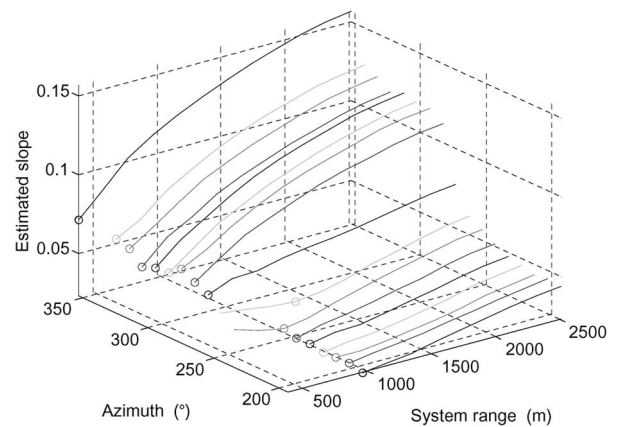


Fig. 14. Estimated RMS slope as a function of system range for 17 different azimuth directions for data set B. Minima are indicated with circles.

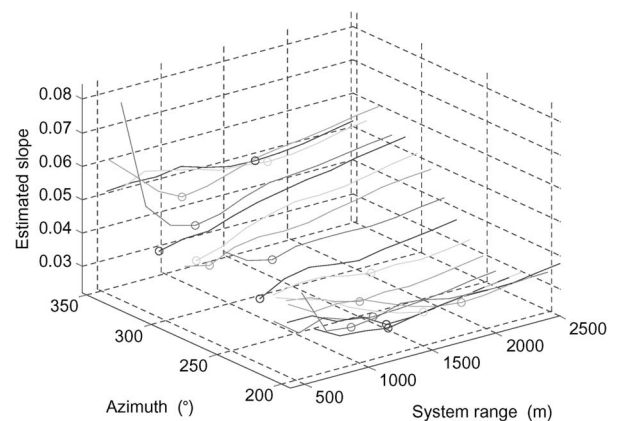


Fig. 15. Estimated RMS slope as a function of system range for 17 different azimuth directions for data set A. Minima are indicated with circles.

cases, provide a reasonable estimate of the minimum. This may be the case when the relation between the system range and  $\sigma_{RMS}$  is smooth, as in Fig. 14, and can be approximated by a second-order polynomial. Extrapolating this polynomial toward zero system range may help to obtain a reasonable estimate of  $\sigma_{RMS}$ . For comparison, the dependence between system range and  $\sigma_{RMS}$  for data set A is shown in Fig. 15.



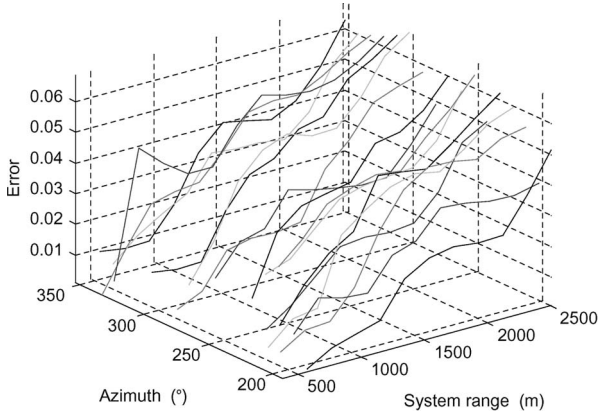


Fig. 16. RMS error in Smith function fit as a function of system range for 17 different azimuth directions for data set A.

A more sophisticated method for selecting the system range should be considered in future work, although the current method provides reasonable estimates for data considered up to now. This may include a study of raw radar images, and it may also be necessary to take wind data into account. The minimum slope value is not necessarily an optimal criterion. It may cause the algorithm to select a too low system range in some situations, and hence, basing the  $\sigma_{\text{RMS}}$  estimates on less data than actually available. A few alternatives have been already tested during this work.

- The relation between RMS errors in the Smith function fit and system range (see Fig. 16) has been investigated. So far, however, it seems to be more difficult to define an automatic algorithm for estimating the system range based on this relation than using the connection between slope and system range. This can be partly understood by comparing Fig. 15 to Fig. 16, in which it seems easier to automatically detect minima in Fig. 15 rather than the flattening tendencies or inflection points in Fig. 16.
- The system range algorithm already developed for the Miros Wavex and Oil Spill Detection system [24] has been tested during this work, but the criteria used there are too weak to ensure a reliable fit of Smith's function.

Another challenge typical for situations with low wind speeds is the lack of shadowing in the images. The data available for this work have been acquired at Veslefrikk [25] with an average antenna height of 43.2 m, which is relatively high compared to typical installations of such navigation radars. This height and the corresponding grazing angles imply less shadowing in the images than for a more typical installation with an antenna height of 20–30 m. Data are currently being collected at an alternative site with a lower antenna height for the purpose of testing this algorithm on more typical (and favorable) data.

2) *Tidal Compensation*: The average antenna height at Veslefrikk is 43.2 m above the mean sea level. Veslefrikk is a platform standing on the seabed, and hence, the distance between the radar antenna and the sea level is influenced by tidal variations. Tidal variations during the period of interest are  $\pm 0.8$  m relative to the mean sea level. These variations are taken into account when calculating local grazing angles in the images by means of data from a Miros Range Finder [26] measuring the air gap between the radar antenna and the

sea level. Without such compensation, the system accuracy would be influenced by tidal variations. The sensitivity for uncompensated tidal variations depends on the sea state and the absolute antenna height. For systems installed on floating vessels with varying loads, it is equally important to compensate for variations in the antenna height above the sea surface related to varying draught.

#### D. Estimation of Significant Wave Height $H_{m0}$

The slope (or steepness)  $\sigma$  of a periodic wave train is generally defined as the crest-to-trough height/wavelength [15]. Assuming deep water and substituting the wavelength with period  $T$ , the general surface slope can be expressed by [15] and [16]

$$\sigma = \frac{2\pi H}{gT^2} \quad (13)$$

where  $H$  represents a wave height, and  $g$  is the gravitational acceleration. A frequently used relation is [16] and [15] given by

$$\sigma_s = \frac{2\pi H_{m0}}{gT_{m02}^2} \quad (14)$$

in which  $\sigma_s$  is the significant slope, and  $T_{m02}$  is the mean zero up-crossing period. Note that deep water is not a requirement for the algorithm developed in this work. The deep water assumption is merely made to simplify the mathematical notation by avoiding using the full dispersion relation.

The relation between significant wave height  $H_{m0}(=H_s)$  and RMS wave height  $H_{\text{RMS}}$  is given by [16]

$$H_{m0} = \sqrt{2} H_{\text{RMS}}. \quad (15)$$

Hence, from the general definition of steepness, a similar relation should be valid for slope

$$\sigma_s = \sqrt{2} \sigma_{\text{RMS}}. \quad (16)$$

Thus, by combining (14) and (16), rearranging, and then using the average RMS slope  $\sigma_{\text{RMS}}^A$  from (12) to utilize information from all available azimuth directions, the significant wave height is calculated by

$$H_{m0} = \frac{\sigma_{\text{RMS}}^A g T_{m02}^2}{\sqrt{2}\pi}. \quad (17)$$

$T_{m02}$  can be estimated from wave spectra obtained by processing these X-band radar sea surface images using already existing methods [1] and [15]. Thus, the algorithm described here does not require information from a reference sensor to be calibrated. To obtain the results presented here, however,  $T_{m02}$  estimates from a reference sensor were used. This sensor is based on a different measurement principle and provides very high accuracy, which was considered necessary as the development work was at a stage where controlling various sources of inaccuracy was very important.

1) *Directional Dependence*: The shadowing rate and the estimates of  $\sigma_{\text{RMS}}$  depend on the wind and wave direction. This implies that the  $H_{m0}$  estimate may be biased if the  $\sigma_{\text{RMS}}^A$  estimate is not based on a representative set of image sectors from various azimuth directions. This directional dependence

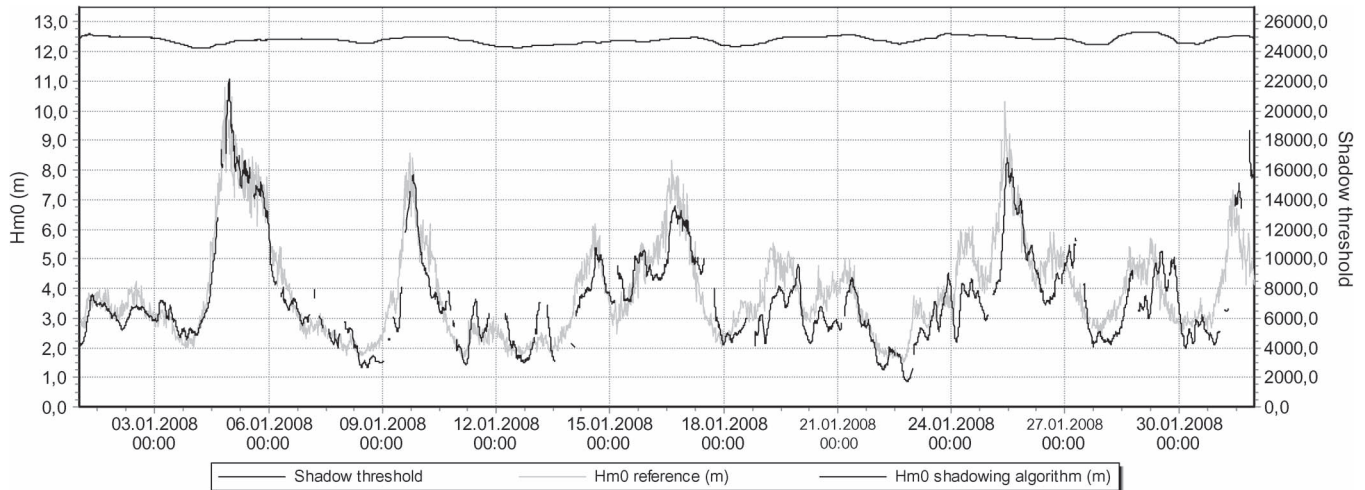


Fig. 17. Time series of  $H_{m0}$  values from the shadowing algorithm (black, left axis) compared to the reference data (gray, left axis) and the estimated shadow threshold used to separate the raw radar images into shadow and no shadow (black, right axis).

will be more significant in situations with high wind speeds and high waves due to increasing influence from nonlinear effects. Directional dependence may be an important subject for future research.

#### E. Precipitation Detection

Data with significantly reduced quality due to precipitation are automatically disregarded using methods based on minimum signal levels in local image areas [27]. These minimum levels are usually associated with shadowed areas. During periods of precipitation, however, the minimum levels increase because the precipitation reflects some of the electromagnetic power back to the antenna.

#### F. Vessels, Land, and Other Objects

Vessels, land, and remaining objects influencing on the image statistics should be removed before applying the shadowing algorithm. Such functionality has, however, not been employed in this work because no disturbing objects were present during the period of interest.

### III. RESULTS

A time series of  $H_{m0}$  estimates is shown in Fig. 17 (black line) after reprocessing raw radar images acquired at Veslefrikk [25] in January 2008 with the algorithm described in the previous sections. All available data are shown, apart from data automatically excluded by the precipitation detection algorithm [27] and data automatically disregarded due to unsuccessful fit of Smith's function. Reference data are available from a Miro Range Finder [26] at the same site (gray line). A scatter plot based on the same data, comparing  $H_{m0}$  estimates from the shadowing algorithm to reference data, is shown in Fig. 18.

For some periods, the results from the shadowing algorithm comply reasonably well with the reference sensor, whereas for other periods, relatively large deviations can be observed. The deviations can be partly explained by the results being based on two different measurement principles: The range finder measures the sea surface elevation in one single point, whereas the shadowing algorithm averages statistics from a large image

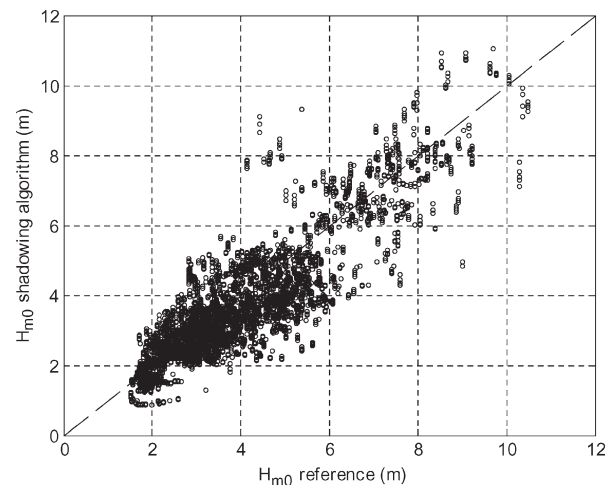


Fig. 18. Scatter plot comparing  $H_{m0}$  values from the shadowing algorithm to the reference data.

area. The scatter plot (see Fig. 18) shows that the results from the new algorithm are reasonably well distributed around those of the range finder without any significant bias. The correlation coefficient is 0.87.

The shadow threshold estimate is fairly stable during the entire month of data (black line, right axis). Its value is close to the threshold that we might manually define by visual inspection, and it produces  $H_{m0}$  values with a reasonable average level and dynamics. The only data sets excluded for estimating the threshold are those being automatically tagged by the precipitation detection algorithm. The method for shadow threshold estimation seems to be robust also for data sets with weak sea backscatter caused by low wind speeds. This robustness can be explained: When the statistics of image pixels located between shadow and no shadow are calculated, areas with weak backscatter are automatically disregarded. Sharp edges are blurred or totally removed in such areas.

### IV. SUMMARY AND CONCLUSION

A novel algorithm that produces reasonable  $H_{m0}$  estimates based on shadowing in sea surface images has been developed.



The method is deeply rooted in theory and does not depend on any reference measurements, meaning that it is self-calibrating. This has not been the case for any known calibration method up to now. The algorithm produces reasonable results, although the method still has several remaining issues that should be looked deeper into. Some important tasks that should be subject for future work are the following:

- Examining the  $H_{m0}$  estimate dependence on the direction of sight relative to wind and wave direction.
- Does the system require a normalization procedure for azimuth and range resolution in the images before applying edge detection?
- A more sophisticated method for estimating the system range may be of importance.
- Considering partial shadowing when working with data from other sites may be necessary.
- Functionality to handle noise lines, vessels, land, and remaining objects in the images should be included if necessary.

#### ACKNOWLEDGMENT

The author would like to thank V. S. Bertelsen, Ø. Grønlie, A. Storhaug, and E. S. Andersen for their valuable input and support, as well as useful discussions, both with regard to technical and literary work, and also the Norwegian company Statoil for allowing data from their site to be used for this work.

#### REFERENCES

- [1] V. Atanassov, W. Rosenthal, and F. Ziemer, "Removal of ambiguity of two-dimensional power spectra obtained by processing ship radar images of ocean waves," *J. Geophys. Res.*, vol. 90, no. C1, pp. 1061–1067, Jan. 1985.
- [2] I. R. Young, W. Rosenthal, and F. Ziemer, "A three-dimensional analysis of marine radar images for the determination of ocean wave directionality and surface currents," *J. Geophys. Res.*, vol. 90, no. C1, pp. 1049–1059, Jan. 1985.
- [3] Ø. Grønlie, "WAVEX—Principles of operation," Miros, Asker, Norway, Oct. 2009, 1399/DD/011 rev. 03.
- [4] J. Seemann, F. Ziemer, and C. M. Senet, "A method for computing calibrated ocean wave spectra from measurements with a nautical X-band radar," in *Proc. MTS/IEEE Conf. OCEANS*, Halifax, NS, USA, Oct. 1997, vol. 2, pp. 1148–1154.
- [5] J. C. Nieto-Borge, K. Hessner, P. Jarabo-Amores, and D. de la Mata-Moya, "Signal-to-noise ratio analysis to estimate ocean wave heights from X-band marine radar image time series," *IET Radar Sonar Navig.*, vol. 2, no. 1, pp. 35–41, Feb. 2008.
- [6] R. Gangeskar, "Wave height derived by texture analysis of X-band radar sea surface images," in *Proc. IEEE IGARSS*, Honolulu, HI, USA, 2000, vol. 7, pp. 2952–2959.
- [7] R. Gangeskar, "An adaptive method for estimation of wave height based on statistics of sea surface images," in *Proc. IEEE IGARSS*, Honolulu, HI, USA, 2000, vol. 1, pp. 255–259.
- [8] L. B. Wetzel, "Electromagnetic scattering from the sea at low grazing angles," in *Surface Waves and Fluxes*. Boston, MA, USA: Kluwer, 1990, pp. 109–172.
- [9] M. D. Henschel, J. R. Buckley, and F. W. Dobson, "Estimates of wave height from low incidence angle sea clutter," presented at the Proc. 4th Int. Conf. Wave Hindcast. Forecast., Banff, AB, Canada, Oct. 1995, E-3.
- [10] J. R. Buckley and J. Aler, "Estimation of ocean wave height from grazing incidence microwave backscatter," in *Proc. IEEE IGARSS*, Singapore, 1997, vol. 2, pp. 1015–1017.
- [11] J. R. Buckley and J. Aler, "Enhancements in the determination of ocean surface wave height from grazing incidence microwave backscatter," in *Proc. IEEE IGARSS*, Seattle, WA, USA, 1998, vol. 5, pp. 2487–2489.
- [12] J. R. Buckley, "Can geometric optics fully describe radar images of the sea surface at grazing incidence?" in *Proc. IEEE IGARSS*, Sydney, Australia, 2001, vol. 4, pp. 1732–1734.
- [13] W. J. Plant and G. Farquharson, "Wave shadowing and modulation of microwave backscatter from the ocean," *J. Geophys. Res.*, vol. 117, no. C8, pp. C08010-1–C08010-17, Aug. 2012.
- [14] B. G. Smith, "Geometric shadowing of a random rough surface," *IEEE Trans. Antennas Propag.*, vol. AP-15, no. 5, pp. 668–671, Sep. 1967.
- [15] M. J. Tucker and E. G. Pitt, *Waves in Ocean Engineering*. Amsterdam, The Netherlands: Elsevier, 2001.
- [16] *Guide to Wave Analysis and Forecasting*, Secretariat of the World Meteorological Organization, Geneva, Switzerland, 1998, World Meteorol. Org.
- [17] V. S. Bertelsen, private communication, 2010.
- [18] W. K. Pratt, *Digital Image Processing*. Hoboken, NJ, USA: Wiley, 1991, pp. 497–518.
- [19] A. Rosenfeld and A. C. Kak, *Digital Image Processing Vol II*, 2nd ed. New York, NY, USA: Academic, 1982, pp. 152–190.
- [20] J. S. Weska, R. N. Nagel, and A. Rosenfeld, "A threshold selection technique," *IEEE Trans. Comput.*, vol. C-23, no. 12, pp. 1322–1326, Dec. 1974.
- [21] R. Gangeskar, "Removal of interference noise lines from X-band radar images. Measuring directional wave spectra and sea surface currents with a marine navigation radar," Ph.D. dissertation, Dept. Phys., Univ. Oslo, Oslo, Norway, 2001.
- [22] C. Bourlier, G. Berginc, and J. Saillard, "One- and two-dimensional shadowing functions for any height and slope stationary uncorrelated surface in the monostatic and bistatic configurations," *IEEE Trans. Antennas Propag.*, vol. 50, no. 3, pp. 312–324, Mar. 2002.
- [23] J. C. Lagarias, J. A. Reeds, M. H. Wright, and P. E. Wright, "Convergence properties of the Nelder–Mead simplex method in low dimensions," *SIAM J. Optim.*, vol. 9, no. 1, pp. 112–147, 1998.
- [24] R. Gangeskar, "Description of new algorithm for estimation of system operating range," Miros, Asker, Norway, 3203/TN/010, Dec. 2006.
- [25] V. S. Bertelsen, "A comparison of Wavex with wave data from a Miros Range Finder SM-094," Miros, Asker, Norway, 1300/TE/009, Sep. 2010.
- [26] H. Feiring, *Miros Microwave Range Finder SM-094/2—Technical Handbook*. Asker, Norway: Miros, Mar. 2007, 1201/TH/004.
- [27] V. S. Bertelsen, private communication, 2012.



**Rune Gangeskar** was born in Oslo, Norway, in 1969. He received the Cand.Scient. and Dr.Scient. degrees in physics and instrumentation from the University of Oslo, Oslo, Norway, in 1995 and 2002, respectively.

From 1995 to 1998, he was a Research Scientist with SINTEF Electronics and Cybernetics. Since 1998, he has been with Miros AS, Asker, Norway, first as a Research Fellow in 1998–2002, then as a Research Scientist in 2002–2006, and since 2006 as a Consultant, developing algorithms for various radar-based systems measuring environmental data at sea. Since 2006, he has been with Tronrud Engineering AS, Ringerike, Norway, as a Research Scientist, developing products and business related to various industries, with a particular focus on technologies related to solar cells, renewable energy, and medical technology. The work includes participation at international conferences and in various research projects, in-house-training, mathematical modeling, and specific R&D work oriented toward new and existing products.